The intersystem crossing of a cyclic (alkyl)(amino) carbene gold (i) complex

S. Thompson, J. Eng, and T. J. Penfold

Citation: The Journal of Chemical Physics **149**, 014304 (2018); doi: 10.1063/1.5032185
View online: https://doi.org/10.1063/1.5032185
View Table of Contents: http://aip.scitation.org/toc/jcp/149/1
Published by the American Institute of Physics

The intersystem crossing of a cyclic (alkyl)(amino) carbene gold (I) complex

S. Thompson, J. Eng,[a] and T. J. Penfold[b]
Chemistry, School of Natural and Environmental Sciences, Newcastle University, Newcastle upon Tyne NE1 7RU, United Kingdom

(Received 3 April 2018; accepted 11 June 2018; published online 5 July 2018)

The intersystem crossing (ISC) mechanism of a cyclic (alkyl)(amino) carbene gold (I) complex (**CMA1**) is studied using quantum dynamics. A model spin-vibronic Hamiltonian is developed, which includes 10 excited states and two important nuclear degrees of freedom. The quantum dynamics reveals that ISC from $S_1 \rightarrow T_1$ occurs on the tens of picosecond time scale, consistent with recent experiments. It is driven by motion along the torsional degree of freedom of the carbazole (Cz) ligand, which causes orthogonality between the donor and acceptor groups closing the gap between the initial (S_1) and final (T_1) states. The role of higher triplet states through spin-vibronic interactions is also discussed. Although previous calculations, evaluated in the Condon approximation, yield large ISC rates, our present dynamical treatment, taking into account the large amplitude torsional motion, increases the calculated rate by an order of magnitude improving the agreement with experiments. The model spin-vibronic Hamiltonian developed can also be used to understand the properties of related linear metal carbene compounds, facilitating molecular design. https://doi.org/10.1063/1.5032185

I. INTRODUCTION

Molecular triplet states represent an important outcome from excited state dynamics, and their presence can be detrimental as well as exploited. Consequently, understanding the mechanism of triplet formation is important for a broad range of molecular systems and not just in molecules containing heavier elements. In the simplest case, intersystem crossing (ISC) is driven by direct spin-orbit coupling (SOC) between two states of different multiplicity. These two states are considered in isolation, and the electronic spin-orbit coupling matrix elements (SOCMEs) are treated independently from the vibrational degrees of freedom, i.e., the Condon approximation.[1] However, many recent time-resolved experiments, especially on transition metal systems, have illustrated that ISC is often not so straightforward.[2,3] Indeed, ISC rates correlated to the vibrational period of important normal modes instead of the heavy atom effect[4] or thermally activated intersystem crossing pathways, which depend upon specific molecular vibrations,[5] have been observed. These results, which signify the breakdown of the Condon approximation, place an emphasis upon explicitly understanding the coupled dynamics of the spin, electronic, and vibrational components occurring within molecular excited states.

The communication between singlet and triplet states is especially important in the context of harvesting the triplet excited states generated upon electrical excitation in organic light emitting diodes (OLEDs). The use of fluorescence emitters limits these devices, by spin-statistics, to a maximum internal quantum efficiency of 25%, as 75% of the excitons are formed in non-radiative triplet states. Although this has been overcome using phosphorescence emitters, this approach relies upon molecules containing rare elements such as iridium and platinum. Recently, Thermally Activated Delayed Fluorescence (TADF) has emerged as a competitive approach and circumnavigates the reliance upon heavy elements. Here, the triplet states are harvested via the singlet states as delayed fluorescence using thermal energy. While a significant amount of the present focus in this area has been upon organic molecules,[6–8] TADF has a strongly established history in Cu(I) complexes[9–11] and has also been reported in Ag(I)[12] and Au(III)[13,14] complexes.

In organic TADF molecules, the mechanism for efficient ISC and reverse ISC (rISC) has been demonstrated to be spin-vibronic[15–19] and, consequently, depends upon specific vibrational degrees of freedom, which increases the mixing between singlet and triplet states. By contrast, for the transition metal TADF systems, the contribution of specific vibrational degrees of freedom has not received the same attention. Recently, Di *et al.*[20] proposed a cyclic (alkyl)(amino) carbene (CAAC) gold (I) complex (**CMA1**, Fig. 1), which exhibits efficient *triplet harvesting* and high performance when incorporated into an OLED device. The authors proposed that the triplet states are harvested by a so-called rotationally assisted spin-state inversion (RASI) mechanism. Here the rapid ISC and rISC were thought to arise because the S_1 state falls below the T_1 state along the main reaction coordinate involving a torsion around the Au–N_2 bond (φ, Fig. 1) creating an

[a]Electronic mail: Julien.Eng@ncl.ac.uk.
[b]Electronic mail: Tom.Penfold@ncl.ac.uk.

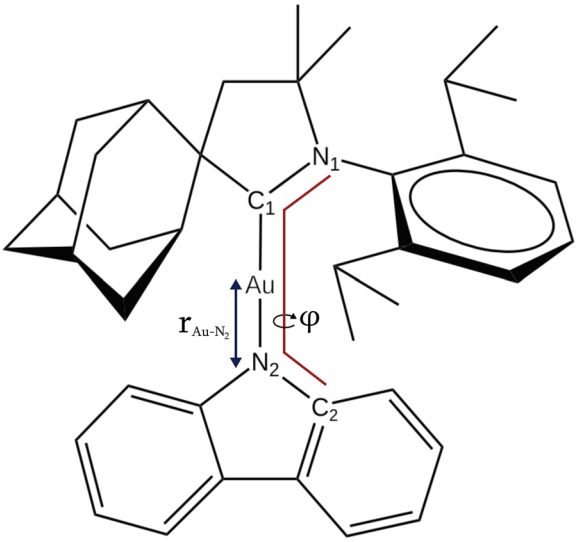

FIG. 1. Schematic of the cyclic (alkyl)(amino) carbene gold (I) complex (**CMA1**) studied herein. The stretching (r_{Au-N_2}) and torsional (φ) degrees of freedom important in the quantum dynamics simulations are highlighted.

intersection between the states. This interpretation was supported by the observation that triplet harvesting was less effective in polycrystalline powders, which the authors proposed was due to the steric hindrance of φ. However, this mechanism is at odds with quantum mechanics, which states that a singlet and triplet state of the same character cannot cross. Indeed, within the one-electron limit, the two states are split by two times the exchange energy, which lowers the energy of the triplet state and lifts the energy of the singlet state.[21]

Recently Föller and Marian[22] demonstrated that this proposed mechanism was founded upon the incorrect simultaneous use of unrestricted density functional theory (uDFT) and time-dependent density functional theory (TDDFT). Using quantum chemical calculations based upon the combined density functional theory and multireference configuration interaction (DFT/MRCI),[23,24] they showed that ordering of the S_1 and T_1 states does not invert along the torsional reaction coordinate. Instead it was proposed that the efficient equilibration between the S_1 and T_1 states was possible without invoking the RASI mechanism. The red shift in the luminescence spectrum of **CMA1** in solution was assigned to a solvent reorganisation following a significant change in the dipole moment associated with excitation into a charge transfer (CT) state, i.e., the solvent adapting to the new electronic structure of excited **CMA1**.

This previous work highlights that the RASI mechanism cannot be correct; however, the rapid ISC and rISC reported in this complex and the high external quantum efficiencies for OLED devices mean that it represents an interesting material for such applications. In this present contribution, we use quantum dynamics simulations to provide detailed insight into the excited state dynamics of **CMA1**. By developing a model spin-vibronic Hamiltonian, we show that although previous calculations[22] evaluated in the Condon approximation yield large ISC rates, our present dynamical treatment, taking into account the large amplitude torsional motion, increases this rate by an order of magnitude improving the agreement with experimental observations. Vibronic coupling to the higher lying triplet states appears to primarily alter the rISC process, although, in contrast to organic TADF systems, it is a detrimental effect due to the interference with the direct ISC pathways. The model spin-vibronic Hamiltonian developed is also general and consequently can straightforwardly be adapted to understand the properties of related linear metal carbene compounds, facilitating molecular design.

II. METHODS

A. Quantum chemistry

Geometry optimisations were performed using DFT and TDDFT for the ground and excited states, respectively, as implemented within the Q-Chem quantum chemistry package.[25] The PBE0 exchange and correlation functional[26] was used, and the def2-SVP basis set[27] was employed for all atoms. The corresponding electronic core potential (ECP)[28] was used for gold. All optimisations were performed in the gas phase.

The excited state properties of **CMA1** were calculated using TDDFT(PBE0) and the def2-TZVP basis set[27] with the associated ECP[28] for gold. The Tamm-Dancoff approximation (TDA)[29] was employed to avoid the over-stabilisation of low lying intra-ligand triplet states. The solvent has been modelled with the conductor-like screening model (COSMO) approach.[30] Emission energies were calculated using the state-specific solvation approach as implemented within Q-Chem; i.e., both the fast (electronic) and slow (nuclear) components of the solvation model have been relaxed to accommodate the considered excited state.[31] Spin-orbit coupling was computed using the ADF software suite[32–34] using the zero order regular approximation (ZORA).[35–37] These calculations were performed at the TDDFT(PBE0) level using a double-ζ polarized basis set[38–40] for hydrogens and a triple-ζ polarised basis set[38–40] for all other atoms.

B. Spin-vibronic Hamiltonian and quantum dynamics

To study the excited state intersystem crossing mechanism of **CMA1**, we adopt a 2-dimensional model spin-vibronic Hamiltonian.[41–43] The present model spin-vibronic Hamiltonian includes the three lowest excited triplet states and the lowest excited singlet state (S_1). Each of the three M_s components has been explicitly included, meaning that the Hamiltonian contains 10 excited states.

The two nuclear degrees of freedom are the torsion around the Au–N_2 bond (φ) and the stretching mode (r_{Au-N_2}) of the same bond. Both motions are responsible for tuning the energy of the CT states. For the former, motion along this mode changes the relative energy gap between the S_1 and T_1 states, while motion along the latter (r_{Au-N_2}) modifies the energy gap between the CT states and the higher lying ligand centred excitations. While structural changes for the latter are small, the 1/R dependency of the energy of CT states with respect to the separation of the donor and acceptor groups (R) means it still plays an important role in the dynamics. Finally, we assume,

consistent with experimental observations, that the initial geometric relaxation, occurring mostly in the CAAC ligand on the femtosecond time scale, plays a minimal role in the ISC which occurs on a much longer time scale, and therefore all dimensions not included in the Hamiltonian are at the minimum of S_1 geometry.

The Hamiltonian operator is expressed as

$$\mathcal{H} = \mathbf{T_N} + \mathbf{W}, \tag{1}$$

where $\mathbf{T_N}$ and $\mathbf{W}$ are the kinetic and potential energy operators, respectively, and are defined in Subsections II B 1–II B 3.

1. The kinetic energy operator

The form of the kinetic energy operator (KEO) depends on the coordinates chosen. Herein we adopt a KEO expressed as a sum of two uncoupled monodimensional KEOs,

$$\mathbf{T_N} = -\frac{1}{2I}\frac{\partial^2}{\partial\varphi^2} - \frac{1}{2\mu}\frac{\partial^2}{\partial r^2_{Au-N_2}}. \tag{2}$$

The first term is the kinetic energy operator of the rotation of a solid top, where I is the moment of inertia,

$$I = \sum_i m_i r_i^2, \tag{3}$$

where i denotes all atoms of the rotating carbazole ligand, m_i denotes their mass, and r_i denotes their distance to the rotation axis. The second term in the kinetic energy operator is associated with r_{Au-N_2}, with μ being the reduced mass of the system,

$$\mu = \frac{(\sum_A m_A)(\sum_B m_B)}{\sum_A m_A + \sum_B m_B}, \tag{4}$$

where A and B denote the atoms of the Cz moiety and of the CAAC ligand including the gold atom, respectively, and m_A, m_B denote their respective mass. The parameters of the kinetic energy operator are I = 3003.84 amu.a_0^2 and μ = 128.91 amu. The implicit assumption in Eq. (2) is that the motion of φ and r_{Au-N_2} are decoupled. This represents a valid approximation because r_{Au-N_2} is also the axis of rotation for φ. Consequently, the stretching motion does not change the distance of the Cz ligand atoms to the rotation axis, thus the moment of inertia I is independent with respect to r_{Au-N_2}.

2. The potential

The potential energy component of the Hamiltonian, $\mathbf{W}$, is expressed as

$$\mathbf{W} = \mathbf{W^{vib}} + \mathbf{W^{soc}}, \tag{5}$$

where $\mathbf{W^{vib}}$ contains the diabatic electronic states and the coupling between them, while $\mathbf{W^{soc}}$ contains the SOCME in the diabatic picture. They are obtained by transformation of the computed SOCME between the so-called electronic adiabatic states ($\mathbf{V^{SOC}}$). If $\mathcal{R}$ be the adiabatic to diabatic rotation matrix that transforms the adiabatic electronic states $\mathbf{V}$ into the diabatic electronic states matrix $\mathbf{W^{vib}}$ through the transformation

$$\mathbf{W^{vib}} = \mathcal{R}^{-1}\mathbf{V}\mathcal{R}. \tag{6}$$

$\mathbf{W^{soc}}$ is then obtained through the same rotation,

$$\mathbf{W^{soc}} = \mathcal{R}^{-1}\mathbf{V^{soc}}\mathcal{R}. \tag{7}$$

The vibronic coupling occurs between electronic states of the same spin multiplicity; $\mathbf{W^{vib}}$ can therefore be written as

$$\mathbf{W^{vib}} = \begin{pmatrix} \mathbf{E_{T_1}} & \boldsymbol{\lambda}^{\mathbf{T1,T2}} & \boldsymbol{\lambda}^{\mathbf{T1,T3}} & 0 \\ \boldsymbol{\lambda}^{\mathbf{T1,T2}} & \mathbf{E_{T_2}} & \boldsymbol{\lambda}^{\mathbf{T2,T3}} & 0 \\ \boldsymbol{\lambda}^{\mathbf{T1,T3}} & \boldsymbol{\lambda}^{\mathbf{T2,T3}} & \mathbf{E_{T_3}} & 0 \\ 0 & 0 & 0 & \mathbf{E_{S_1}} \end{pmatrix}, \tag{8}$$

with E_{T_n} and E_{S_1} being the diabatic potential energy for the triplet and S_1 states, respectively, and $\lambda^{Tn,Tm}$ is the vibronic coupling between the T_n and T_m states. $\mathbf{W^{soc}}$ is written as

$$\mathbf{W^{soc}} = \begin{pmatrix} 0 & \eta^{\mathbf{T1,T2}} & \eta^{\mathbf{T_1,T_3}} & \eta^{\mathbf{T_1,S_1}} \\ \eta^{*\mathbf{T_1,T_2}} & 0 & \eta^{\mathbf{T_2,T_3}} & \eta^{\mathbf{T_2,S_1}} \\ \eta^{*\mathbf{T_1,T_3}} & \eta^{*\mathbf{T_2,T_3}} & 0 & \eta^{\mathbf{T_3,S_1}} \\ \eta^{*\mathbf{T_1,S_1}} & \eta^{*\mathbf{T_2,S_1}} & \eta^{*\mathbf{T_3,S_1}} & 0 \end{pmatrix} \tag{9}$$

with

$$\eta^{\mathbf{T_n,T_m}} = \begin{pmatrix} \mathcal{I}(\eta') & -\mathcal{R}(\eta) + \mathcal{I}(\eta) & 0 \\ -\mathcal{R}(\eta) + \mathcal{I}(\eta) & 0 & \mathcal{R}(\eta) + \mathcal{I}(\eta) \\ 0 & \mathcal{R}(\eta) + \mathcal{I}(\eta) & \mathcal{I}(\eta') \end{pmatrix} \tag{10}$$

and

$$\eta^{\mathbf{T_n,S_1}} = \begin{pmatrix} \mathcal{R}(\eta) + \mathcal{I}(\eta) \\ \mathcal{I}(\eta') \\ \mathcal{R}(\eta) - \mathcal{I}(\eta) \end{pmatrix}, \tag{11}$$

where $\mathcal{R}(\eta)$ and $\mathcal{I}(\eta)$ are the real and imaginary parts of the SOCMEs. In the present model, we consider them as constant, taking their value at the minimum of the S_1 excited state. The 3×3 matrix in Eq. (10) represents the coupling between each of the M_s components of the triplet states.

$\mathbf{W^{vib}}$ is constructed by a fit to the diabatic electronic states along the r_{Au-N_2} stretch and torsion, φ. The diabatic electronic states and coupling are computed using the diabatisation scheme[44] implemented within Q-chem. The vibronic coupling obtained is quite weak, and therefore the diabatic states should be close to the adiabatic ones. The diabatic potential energy curves along the φ degree of freedom are shown in Fig. 2(b). The potential energy surface (PES) of every states is quite flat, with the exceptions of the two energy barriers located around $\varphi = -30°$ and $\varphi = 155°$, which arise from steric clashes between a hydrogen atom of the Cz ligand and a methyl group of the CAAC moiety. In the present model, they arise from the low dimensionality of our model spin-vibronic Hamiltonian. Indeed, in full nuclear configuration space, it is likely that thermal fluctuations of each coordinates will reduce the effect of this barrier. However, the elongation of the r_{Au-N_2} bond alone is not sufficient to prevent the sterical clash, and additional degrees of freedom are needed in order to do so

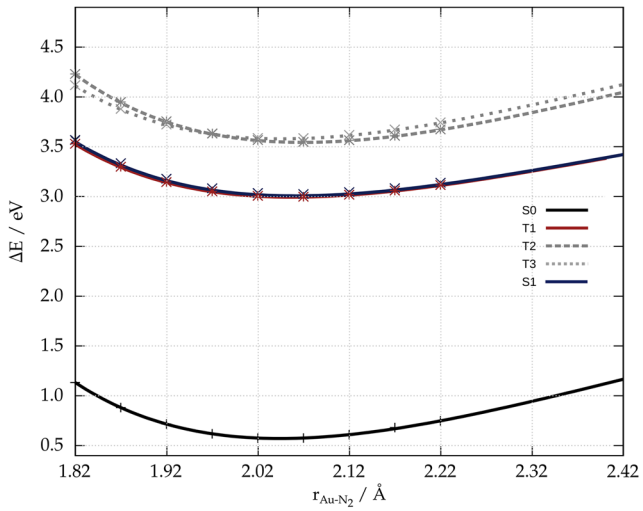

(a)

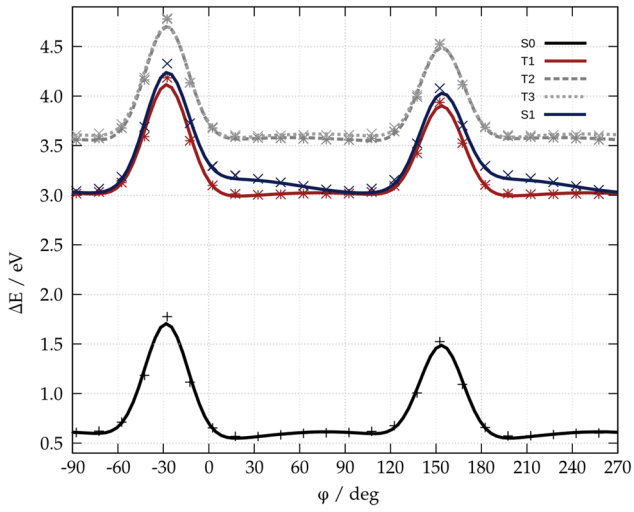

(b)

FIG. 2. Ground state and the four lowest excited diabatic states included in the model spin-vibronic Hamiltonian along (a) r_{Au-N_2} and (b) φ.

and to allow free rotation around the Au–N_2 bond. The implications of this are discussed in the results. All states have been fitted by a sum of sine functions representing the torsion potential and two high order sine functions modeling the steric barriers,

$$E_i(\varphi) = \beta_i \cos(2(\varphi + \tau_i)) + \gamma_i \cos(0.5(\varphi + \psi_i))^{64} + \delta_i \cos(0.5(\varphi + \theta_i))^{64}. \quad (12)$$

The parameters associated with the fits shown in Fig. 2 can be found in Table I.

The vibronic coupling along the torsion is shown in Fig. 3(b). The T_1 and T_2 states are coupled, as well as the T_1 and T_3 states. There is no vibronic coupling between T_2 and T_3 states. The vibronic coupling has been approximated using a sine function,

$$\lambda^{Tn,Tm}(\varphi) = \epsilon \sin(\varphi + \nu), \quad (13)$$

and the parameters of the fits shown in Fig. 3 are shown in Table I.

TABLE I. Parameters resulting from the fit of the diabatic states (top) and vibronic coupling (bottom) along the torsion φ.

Parameter	GS	T_1	S_1	T_2	T_3
β (eV)	−0.047	−0.029	0.070	0.027	−0.033
γ (eV)	0.958	0.945	0.944	0.970	0.951
δ (eV)	1.174	1.158	1.161	1.184	1.166
τ	0.422	0.262	−0.0311	0.548	0.290
ψ	0.458	0.456	0.457	0.4555	0.456
θ	3.629	3.624	3.625	3.625	3.625

Parameter	$T_1 - T_2$	$T_1 - T_3$
ϵ (eV)	−0.059	−0.073
ν	−1.546	−1.676

The diabatic states at the geometry of the minimum of S_1 along the stretch coordinate r_{Au-N_2} are shown in Fig. 2, left. The Au–N_2 bond length does not lift the degeneracy between S_1 and T_1. However T_2 and T_3 cross at small r_{Au-N_2} distances. The stretch potential is fitted using a Morse potential,

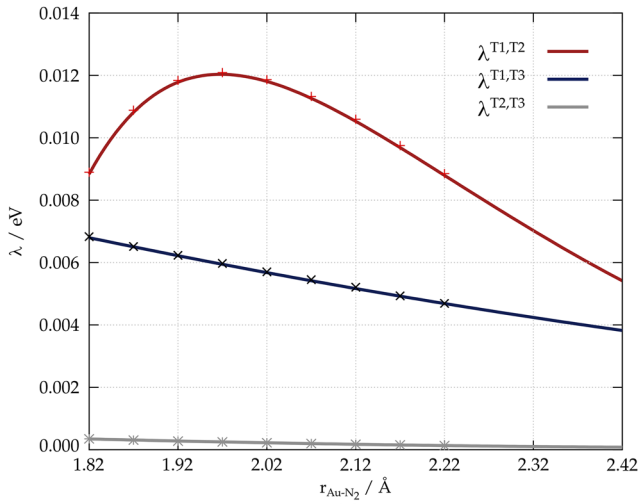

(a)

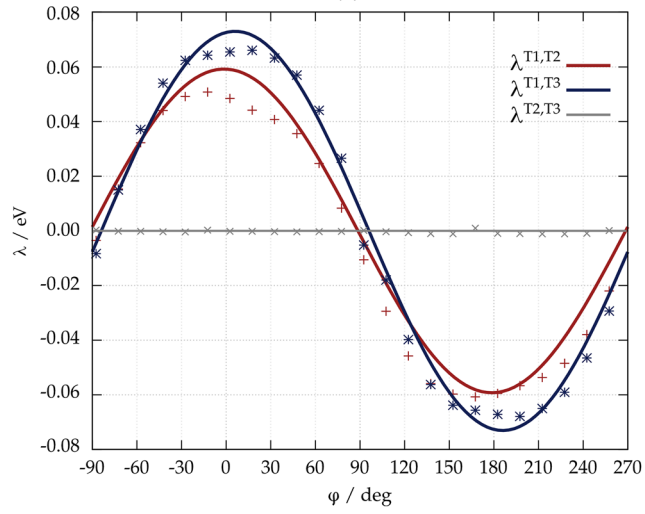

(b)

FIG. 3. Evolution of the vibronic coupling among the triplet manifold along (a) r_{Au-N_2} and (b) φ.

$$E_i(r_{Au-N_2}) = D_i\left(\exp\left(-\alpha(r_{Au-N_2} - r^0_{Au-N_2})\right) - 1\right)^2, \quad (14)$$

where D_i is the dissociation energy, α describes the width of the potential, and $r^0_{Au-N_2}$ is the bond length at the minimum of energy. The parameters of the fit functions are shown in Table II.

The vibronic coupling along r_{Au-N_2} is shown in Fig. 3(a). A second order polynomial expression is sufficient to fit the coupling between T_1 and T_3 (λ^{T_1,T_3}) and between T_2 and T_3 (λ^{T_2,T_3}),

$$\lambda^{T_n,T_m}(r_{Au-N_2}) = a{r_{Au-N_2}}^2 + b r_{Au-N_2} + \lambda^{T_n,T_m}(\varphi_0), \quad (15)$$

where $\lambda^{T_n,T_m}(\varphi_0)$ is the vibronic coupling at equilibrium geometry and is given by the coupling along the torsion φ. However, we need to use a Morse type function to fit properly the largest coupling λ^{T_1,T_2},

$$\lambda^{T_1,T_2}(r_{Au-N_2}) = D_i\left(\exp\left(-\alpha(r_{Au-N_2} - r^0_{Au-N_2})\right) - 1\right)^2 + \epsilon + \lambda^{T_1,T_2}(\varphi_0). \quad (16)$$

The parameters of the fit are shown in Table II.

3. Wavepacket propagation

The quantum dynamics were performed using the multi-configurational time-dependent Hartree (MCTDH) method as implemented within the Quantics quantum dynamics package.[45] The 2-dimensional model spin-vibronic Hamiltonian was represented on a Fast Fourier Transform (FFT) grid of 1001 × 501 grid points for the torsion and the stretching modes, respectively. The torsional mode was set with periodic boundary conditions ranging from $-\pi \rightarrow \pi$. The multi-set formalism was adopted, and 10 single particle functions (SPFs) were used for each mode on the S_1 and T_1 states and 4 SPFs were used for each mode on the T_2 and T_3 states. The evolution of the A-vector was calculated with the constant mean field integration scheme, and the SPFs were propagated with the Runge-Kutta integrator to eighth order (RK8). One initial wavepacket used in the simulations was obtained from a relaxation of a guessed wavepacket upon the ground state surface, vertically projected onto the S_1 surface. For the second set of simulations, a wavepacket with a larger width along the torsional mode was adopted to better represent the distribution of φ associated with the flat nature of the potential along this motion.

In the present spin-vibronic Hamiltonian, no decay channels to the ground state are incorporated and the Hamiltonian is therefore a closed quantum system. Consequently, at longer times, an equilibrium will form between the singlet and triplet states representing the balance between k_{ISC} and k_{rISC}. The population of the S_1 state, in this regime, can be expressed as[19]

$$[S_1(t)] = 1 - \left[\frac{k_{ISC}}{k_{ISC} + k_{rISC}} \times (1 - \exp^{-\{k_{ISC}+k_{rISC}\}t})\right], \quad (17)$$

where $[S_1(t)]$ is the time-dependent population of the S_1 state. This equation is used to fit our population kinetics and extract k_{ISC}. It is noted that this approach can also be used to extract k_{rISC}. However, because our Hamiltonian has 2 dimensions, the energy which passes from the initial electronic excitation into the vibrational degrees of freedom, following decay from the S_1 into the T_1 state, cannot be dissipated. This makes the wavepacket in the T_1 state very vibrationally hot. k_{rISC} is temperature dependent, and so this high nuclear temperature will distort the rISC rate. Consequently, this term arising from our fits is not discussed throughout this work.

TABLE II. Parameters resulting from the fit of the diabatic states (top) and vibronic coupling (bottom) along the vibration r_{Au-N_2}.

Parameter	GS	T_1	T_2	T_3	S_1
D_i (eV)	2.74	1.80	3.40	2.19	1.80
α (Å^{-1})	1.667	1.823	1.380	1.889	1.815
r_{Au-N} (Å)	2.044	2.058	2.068	2.050	2.061
ϵ_i (eV)	0.00	2.42	2.97	3.01	2.44
Parameter	$T_1 - T_2$		Parameter	$T_1 - T_3$	$T_2 - T_3$
D_i (eV)	−0.0134		a (eV Å^{-2})	0.0016	0.0004
α (Å^{-1})	2.6743		b (eV Å^{-1})	−0.0118	−0.0023
r_{Au-N} (Å)	1.9681				
ϵ_i (eV)	−0.0939				

III. RESULTS

A. Excited state properties

The optimised ground-state geometry of **CMA1** adopts the so-called *co-planar* conformation; i.e., the Cz and CAAC ligands are oriented in the same plane (Table III). This can be described using the φ dihedral angle, shown in Fig. 1. The ground state *co-planar* conformation is characterised by $\varphi = 2.9°$. At this geometry, the two lowest triplet excited states (T_1 and T_2) are at 3.05 eV and 3.16 eV. As shown in Table IV, these are both composed of a combination of HOMO → LUMO and HOMO → LUMO+1 transitions. They

TABLE III. Energy of the *co-planar* and *perpendicular* conformations in S_0, S_1, and T_1 and their characteristic values of r_{Au-N_2} and φ.

	Co-planar	*Perpendicular*
S_0		
ΔE (eV)	0.00	0.11
φ (deg)	2.9	87.1
r_{Au-N_2} (Å)	2.05	2.06
S_1		
ΔE (eV)	3.01	2.94
φ (deg)	22.4	89.8
r_{Au-N_2} (Å)	2.11	2.08
T_1		
ΔE (eV)	2.85	2.93
φ (deg)	7.6	85.5
r_{Au-N_2} (Å)	2.07	2.08

TABLE IV. Electronic structure at the geometry of minimum energy in S_0, S_1, and T_1. H represents the HOMO and L represents the LUMO.

S_0 minimum				
State	Excitation	Weight (%)	Osc. str.	Energy (eV)
T_1	$H \rightarrow L$	55	0.000	3.05
	$H \rightarrow L+1$	40		
T_2	$H \rightarrow L$	41	0.000	3.16
	$H \rightarrow L+1$	55		
S_1	$H \rightarrow L$	99	0.178	3.30
T_3	$H-1 \rightarrow L+1$	77	0.000	3.40
S_1 minimum				
State	Excitation	Weight (%)	Osc. str.	Energy (eV)
S_0	...	...	...	0.56
T_1	$H \rightarrow L$	99	0.000	2.97
S_1	$H \rightarrow L$	99	0.001	2.98
T_2	$H \rightarrow L+1$	81	0.000	3.51
T_3	$H-2 \rightarrow L$	95	0.000	3.56
T_1 minimum				
State	Excitation	Weight (%)	Osc. str.	Energy (eV)
S_0	...	...	...	0.35
T_1	$H \rightarrow L$	97	0.000	2.89
S_1	$H \rightarrow L$	99	0.162	3.11
T_2	$H \rightarrow L+1$	96	0.000	3.40
T_3	$H-2 \rightarrow L$	90	0.000	3.57

are therefore a mix of charge transfer from the Cz to the CAAC ligand and a local excitation on the Cz ligand. The third triplet state, T_3, is at 3.40 eV and is a local excitation on the Cz ligand. The absorbing singlet state S_1 falls between the T_2 and T_3 states, at 3.30 eV, and is a pure HOMO → LUMO transition, i.e., a charge transfer state from the Cz to the CAAC ligand. The $S_0 \rightarrow S_1$ absorption of 3.30 eV agrees well with the first peak in the experimental absorption spectrum (~364 nm) and recent calculations, at a higher level of theory by Föller and Marian.[22] The electronic difference densities associated with each of these transitions are shown in Fig. 4.

The *co-planar* arrangement is not the only minimum on the ground state potential energy surface (PES), and the *perpendicular* conformation can also be optimised. The energy difference between the two conformers is only 0.11 eV, highlighting the shallow nature of the potential along the torsional mode of the Cz (φ). To minimise steric hindrance between a hydrogen atom of the Cz ligand and a methyl group of the CAAC moiety, the Au–N_2 bond length is longer than at the *co-planar* minimum, r_{Au-N_2} = 2.06 Å versus r_{Au-N_2} = 2.05 Å. The electronic structure for the *perpendicular* conformation is similar to the one at the *co-planar* geometry.

The T_1 and S_1 potential energy surfaces (PESs) exhibit a similar topology with one minimum at the *co-planar* geometry (φ = 22.4° in S_1, φ = 7.6° in T_1) and another one at a *perpendicular* conformation (φ = 89.8° in S_1, φ = 85.5° in T_1). The *perpendicular* conformation is the most stable in S_1, whereas the *co-planar* conformation is more favourable in T_1. An elongation of the Au–N_2 bond is observed in the *co-planar* minimum of S_1, from r_{Au-N_2} = 2.05 Å in the ground state to r_{Au-N_2} = 2.11 Å in S_1. This reduces the HOMO/LUMO overlap and thus the exchange energy between the electrons. This effect is not observed for the *perpendicular* conformation as the relative orientation of the two ligands already ensures a zero overlap. The exchange energy lowers the energy of the triplet states; therefore, the bond elongation is not observed in T_1. This explains partly why the most stable conformation in S_1 is the *perpendicular* conformation, while the most favourable one in T_1 is the *co-planar* form. At S_1 *co-planar* minimum, the T_1 and S_1 states are nearly degenerate ($\Delta E^{S_1,T_1}$ = 0.01 eV) and both consist of pure HOMO → LUMO transitions. The T_2 is at 3.40 eV and, in contrast to the ground state geometry, is now a pure HOMO to LUMO+1 transition. At this geometry, T_3 is no longer a local excitation on the Cz ligand but is now a local excitation on the CAAC. The difference of electronic density associated with these transitions is shown in Fig. 5. At

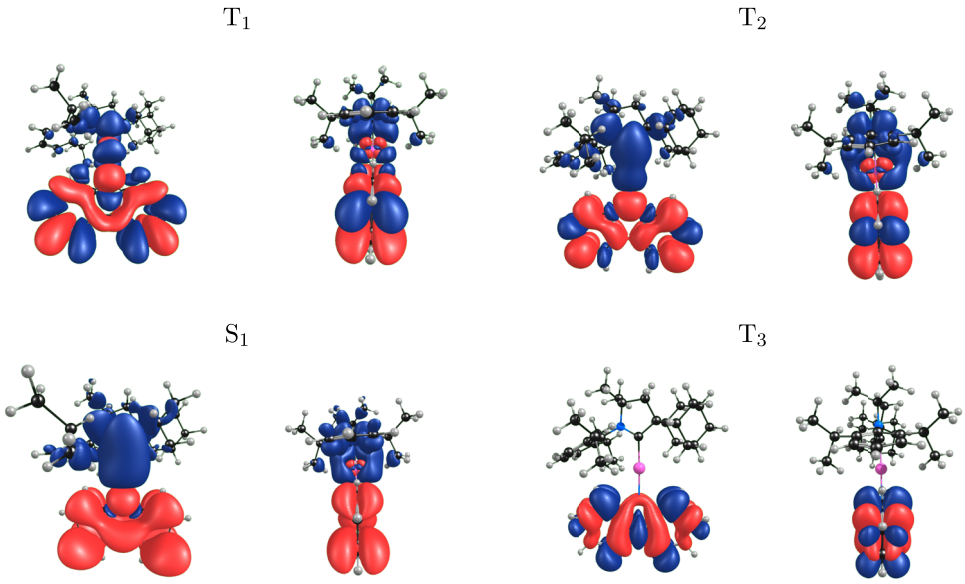

FIG. 4. Difference of electronic density associated with the electronic states T_1, T_2, S_1, and T_3 at the geometry of minimum energy in the ground state of **CMA1**. For each state, front (left) and side (right) views are shown. Loss of electronic density is shown in red; gain is shown in blue.

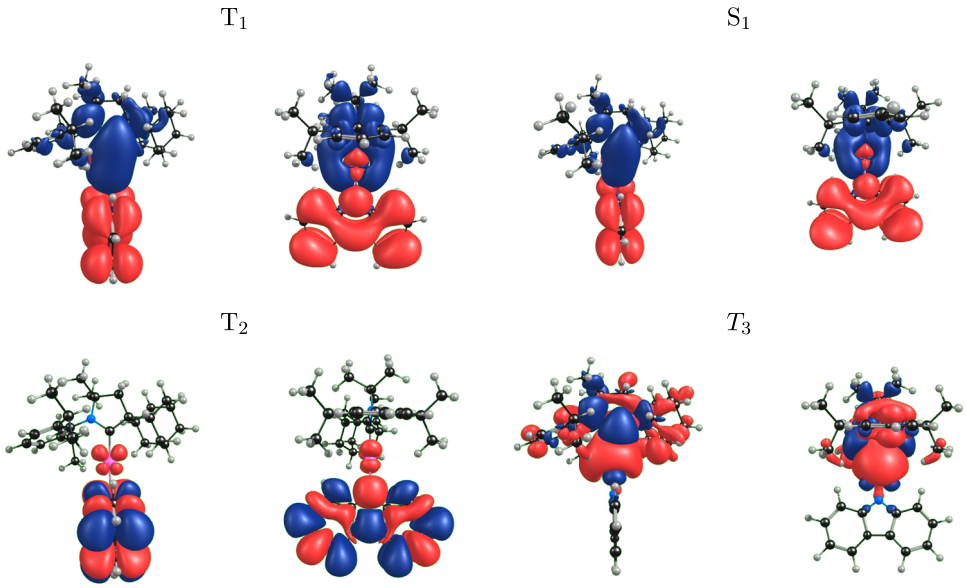

FIG. 5. Difference of electronic density associated with the electronic states T_1, T_2, S_1, and T_3 at the geometry of minimum energy of S_1 of **CMA1**. For each state, front (left) and side (right) views are shown. Loss of electronic density is shown in red; gain is shown in blue.

the S_1 optimised geometry, the S_1 energy is 2.97 eV (417 nm), meaning a Stokes shift of 0.34 eV, which is primarily from the stabilisation of the CAAC ligand, lowering the energy of the LUMO and therefore closing the HOMO-LUMO gap. This exhibits little agreement with the experimental emission spectrum; however, as described by Föller and Marian,[22] this deviation can be accounted for by including the effect of the excited state solvent rearrangement. Using a state-specific continuum model, we find an emission energy of 2.20 eV (563.5 nm) for toluene, in very good agreement with the emission reported experimentally.

In terms of the SOCME, important for coupling the singlet and triplet manifolds, at the S_1 geometry, the T_1 and S_1 states are of the same character and therefore exhibit a relatively small spin-orbit coupling of $\eta^{S_1,T_1} = 13.87\,\mathrm{cm}^{-1}$. In contrast the T_2 state, which consists of a pure local exciton on the CAAC ligand, involves a d orbital of the gold metal. This promotes strong SOC between the T_1 and T_2 and the S_1 and T_2 states of $\eta^{T_1,T_2} = 1393.69\,\mathrm{cm}^{-1}$ and $\eta^{S_1,T_2} = 649.22\,\mathrm{cm}^{-1}$, respectively. The SOCMEs between the low lying states and T_3 are $\eta^{T_1,T_3} = 15.30\,\mathrm{cm}^{-1}$, $\eta^{T_2,T_3} = 26.57\,\mathrm{cm}^{-1}$, and $\eta^{S_1,T_3} = 59.09\,\mathrm{cm}^{-1}$.

B. Quantum dynamics

In this section, we use quantum dynamics in combination with the spin-vibronic Hamiltonian, developed in Sec. II B, to study the ISC dynamics after excitation into the S_1 state. The dynamics are initiated from an initial wavepacket obtained from a relaxation of the wavefunction upon the ground state surface and wider initial wavepacket to account for the distribution in φ expected at room temperature.

Figure 6 shows the S_1 and T_1 population kinetics during the first 100 ps after photoexcitation into the S_1 state when adopting the narrow wavefunction, i.e., the wavefunction obtained from the relaxation. A steady decay of S_1 into the T_1 state is observed throughout the 100 ps of dynamics. At early times, these kinetics are characterised by large amplitude oscillations, which are associated with the initial narrow wavepacket moving along the φ degree of freedom and reaching the point of degeneracy between two states. As described in Sec. II, we use Eq. (17) to extract k_{ISC} and find a value of $2.20 \times 10^{10}\ \mathrm{s}^{-1}$. The dotted light blue line in Fig. 6 shows the same dynamics, but in this case the steric barrier shown in Fig. 2 has been removed, allowing free rotation of the φ torsion. This has the effect of slowing the ISC dynamics

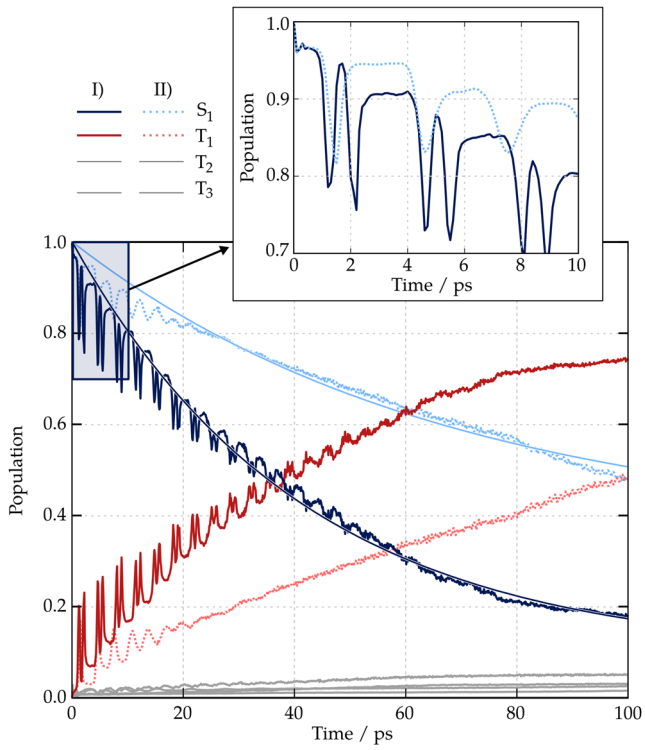

FIG. 6. Evolution of the excited state populations, S_1 (blue) and T_1 (red), with time. Initial wavepacket obtained from a relaxation of the wavefunction on the ground state surface. Full lines (I): Dynamics using the spin-vibronic Hamiltonian described in Sec. II B. Dotted lines (II): Dynamics with no energy barrier along the torsion φ.

slightly, although $k_{ISC} = 9.53 \times 10^9$ s^{-1} remains within a factor of 3.

The population transfer kinetics from S_1 to T_1 exhibits plateaux (Fig. 6, inset). These features are indicative of the fact that the population is transferred principally in the region of near degeneracy (i.e., *perpendicular* geometry) between T_1 and S_1, resulting in "peaks" in the population kinetics. This region is reached for the first time around t = 1250 fs in the presence of steric barriers and at t = 1460 fs for the free rotation. This variation arises from the difference in the gradient of the potential in the vicinity of the *co-planar* conformation. The wavepacket then continues evolving along the torsion φ. In the absence of steric barriers, the periodic torsional coordinates allows free rotation and the wavepacket eventually reaches another region of near degeneracy leading to the next significant transfer of population from S_1 to T_1. The presence of steric barriers prevents such free rotation, and the wavepacket is pushed back and returns to the near degeneracy region leading to the double peak structure. This description is schematically shown in Fig. 7. The frequency of passing of the wavepacket through the near degeneracy region is $\nu_{\text{barrier}} = 2.94 \times 10^{11}$ Hz in the presence of steric barriers and $\nu_{\text{barrierless}} = 1.65 \times 10^{11}$ Hz in their absence. The factor 1.8 between those two frequencies partly explains the difference of k_{ISC} between both simulations. In addition to this effect, the wavepacket lies close to the near degeneracy region when colliding with the steric barrier, allowing for additional population transfer.

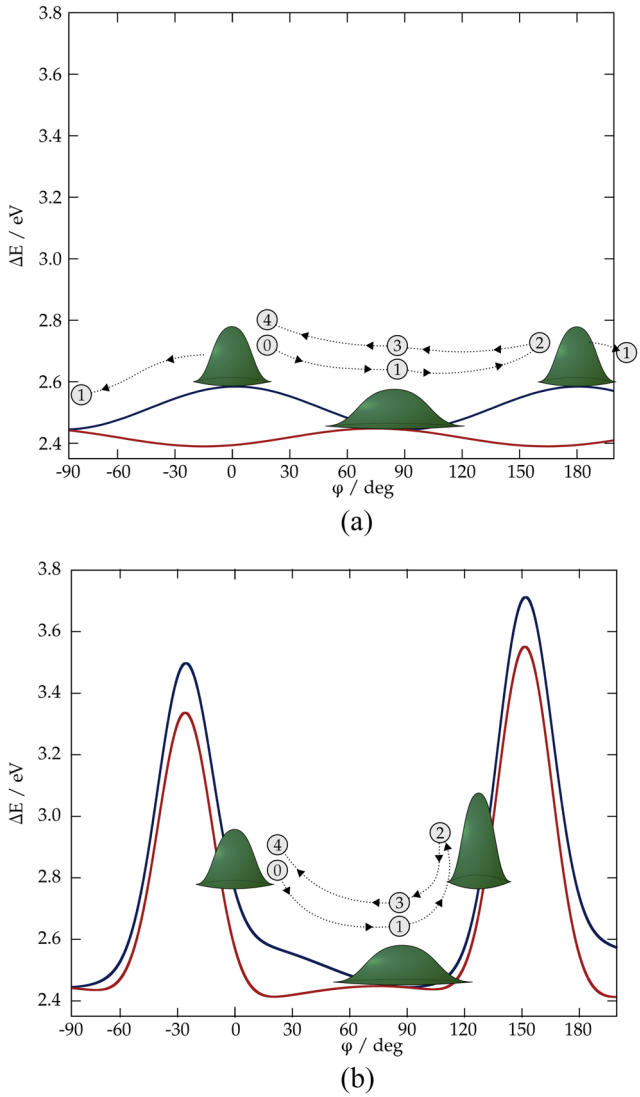

FIG. 7. Schematic representation of the effect of the sterical barrier on the dynamics of the molecular wavepacket (a) in the case of free rotation and (b) in the presence of sterical barriers. Snapshots of the wavepacket at different times are shown with labels from 0 to 4.

Figure 8 shows the S_1 and T_1 population kinetics during the first 100 ps when adopting a wider initial wavepacket. As expected, its largest effect is to damp the large amplitude changes associated with a localised wavepacket meeting the point of degeneracy. This wider wavepacket mimics the large distribution of the φ angle in the ground state expected at room temperature induced by the flat electronic potential of the ground state along the torsion. When reduced, the kinetics still exhibit step changes, which are associated with the simplicity of the 2-dimensional spin-vibronic Hamiltonian, which restricts the flow of vibrational energy to those modes, rather than all vibrational degrees of freedom of the molecule and the solvent, which would provide decoherence. The wider wavepacket only slightly speeds up the rate of intersystem crossing as the wavepacket no longer has to traverse the φ coordinate to undergo ISC. Here we find $k_{ISC} = 2.76 \times 10^{10}$ s^{-1}, and if the steric barrier is removed, $k_{ISC} = 1.37 \times 10^{10}$ s^{-1}. While both of these are in good agreement with the rates reported experimentally, they also demonstrate that the initial choice of wavepacket does not fundamentally alter the interpretation presented herein.

Importantly, in terms of the mechanism of ISC, Fig. 8 also shows the population kinetics for which the coupling with T_2 and T_3 states has been removed. Here we observe a rate of population transfer from S_1 to T_1 of 3.78×10^{11} s^{-1}, in

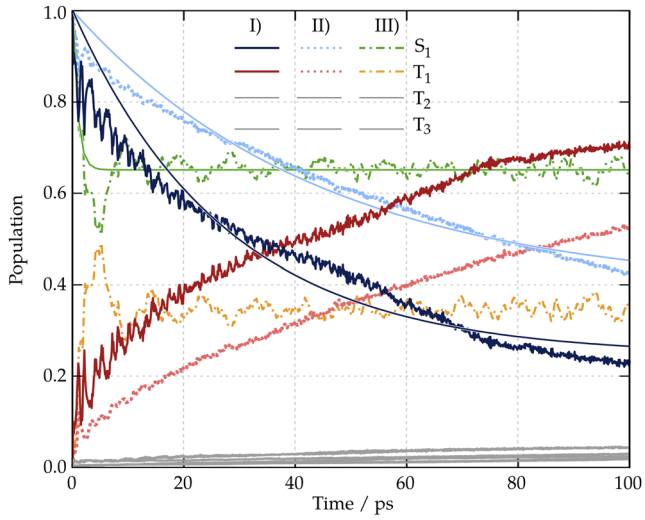

FIG. 8. Evolution of the excited state populations, S_1 (blue) and T_1 (red), with time. A wider initial wavepacket is used to account for the distribution in φ due to the flat potential energy along the torsion φ. Full lines (I): Dynamics using the spin-vibronic Hamiltonian described in Sec. II B. Dotted lines (II): Dynamics with no energy barrier along the torsion φ. Dashed-dotted lines (III): Dynamics without T_2 nor T_3. For clarity purpose, S_1 is shown in green and T_1 is shown in orange.

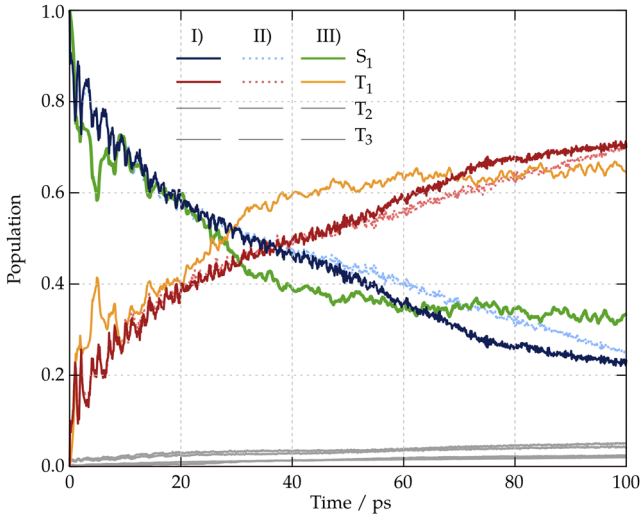

FIG. 9. Evolution of the excited state populations, S_1 (blue) and T_1 (red), with time. (I) Dynamics using the spin-vibronic Hamiltonian described in Sec. II B. (II) Dynamics using the same Hamiltonian without any coupling to T_2. (III) Dynamics using the same Hamiltonian without any coupling to T_3. For the purpose of clarity, S_1 is shown in green and T_1 is shown in orange.

close agreement with the rates observed experimentally and an order of magnitude larger than for the full spin-vibronic Hamiltonian. In addition, a plateau in the population transfer is reached within 20 ps, indicating equilibration between the S_1 and T_1 states and therefore a faster k_{rISC} than for the full Hamiltonian. Figure 9 shows the effect of individual triplet states on the relaxation dynamics. We successively remove each triplet from the Hamiltonian. The absence of T_2 [Fig. 9(II)] or T_3 [Fig. 9(III)] does not prevent the transfer of population from S_1 to T_1, and the relaxation rate is similar to the one obtained from the full Hamiltonian simulation [Fig. 9(I)].

These simulations show that the presence of the T_2 and T_3 modulates the equilibrium ratio of the population in S_1 and T_1 and is therefore indicative of a change in the ratio between the ISC and the rISC rates. Indeed, the presence of at least one of the higher lying states actually suppresses k_{rISC} because equilibrium between the two states is not reached within 100 ps of dynamics. This is in contrast to the observation made for organic TADF systems. This would appear to suggest the role of inferences between the direct ($S_1 - T_1$) and spin-vibronic pathways, i.e., either $T_1 - T_2 - S_1$ or $T_1 - T_3 - S_1$ pathways. These interferences increase ISC from 10^{10} s^{-1} to 10^{11} s^{-1} and provide excellent agreement with the experimentally reported rate of $k_{ISC} = 2.5 \times 10^{11}$ s^{-1} [20] but importantly decreases the k_{rISC}, which is undesirable for high performing OLED devices.

IV. CONCLUSIONS

The present study has used quantum chemistry and quantum dynamics to shed new insight into the excited state properties and intersystem crossing mechanism of **CMA1**. In agreement with recent work,[22] our quantum chemistry confirms that the proposed RASI mechanism[20] is not correct and the lowest singlet and triplet states do not cross.

The quantum dynamics shows that the ISC dynamics occurs on the time scale of tens of picosecond and along the torsional mode, allowing the wavepacket to reach regions of the potential where the singlet and triplet states are degenerate. It is noted that ISC is possible all along the torsional mode but is fastest at the point of degeneracy. Importantly, only a ~30° change in the dihedral is required to get close to the point of degeneracy and therefore using molecular dynamics to observe how much this motion is restricted in the solid state will be important for understanding the operation of **CMA1** in an OLED device.

Our dynamics reveal a spin-vibronic component within the present model with higher lying triplet states. In this case, they act as virtual states in the sense that they contribute to the dynamics, without receiving significant population themselves. This has the strongest influence on k_{rISC} and is indeed expected to slow it down. This arises from interference effects between direct ($S_1 - T_1$) ISC and spin-vibronic pathways, i.e., $T_1 - T_2 - S_1$ or $T_1 - T_3 - S_1$; and the observed behavior is in contrast to organic TADF systems[16–19] as in these cases the direct ISC pathway is very weak.

In summary, this work has provided further insight into the excited state dynamics of **CMA1**. Importantly, the spin-vibronic Hamiltonian developed can be extended to the analogous Cu and Ag systems, which is presently underway.

ACKNOWLEDGMENTS

We acknowledge the EPSRC, Project No. EP/P012167/1, funding. Data supporting this publication are openly available under an "Open Data Commons Open Database License." Additional meta-data are available at 10.17634/162036-1. Please contact Newcastle Research Data Service at rdm@ncl.ac.uk for access instructions.

[1] C. M. Marian, Wiley Interdiscip. Rev.: Comput. Mol. Sci. **2**, 187 (2012).
[2] M. Chergui, Dalton Trans. **41**, 13022 (2012).
[3] T. J. Penfold, E. Gindensperger, C. Daniel, and C. M. Marian, "Spin-vibronic mechanism for intersystem crossing," Chem. Rev. (published online).
[4] A. Cannizzo, A. M. Blanco-Rodriguez, A. El Nahhas, J. Šebera, S. Záliš, A. Vlček, and M. Chergui, J. Am. Chem. Soc. **130**, 8967 (2008).
[5] T. Hofbeck, Y. C. Lam, M. Kalbáč, S. Záliš, A. Vlček, and H. Yersin, Inorg. Chem. **55**, 2441 (2016).
[6] H. Uoyama, K. Goushi, K. Shizu, H. Nomura, and C. Adachi, Nature **492**, 234 (2012).
[7] F. B. Dias, T. J. Penfold, and A. P. Monkman, Methods Appl. Fluoresc. **5**, 012001 (2017).
[8] T. J. Penfold, F. B. Dias, and A. P. Monkman, Chem. Commun. **54**, 3926 (2018).
[9] J. R. Kirchhoff, R. E. Gamache, Jr., M. W. Blaskie, A. A. Del Paggio, R. K. Lengel, and D. R. McMillin, Inorg. Chem. **22**, 2380 (1983).
[10] J. C. Deaton, S. C. Switalski, D. Y. Kondakov, R. H. Young, T. D. Pawlik, D. J. Giesen, S. B. Harkins, A. J. M. Miller, S. F. Mickenberg, and J. C. Peters, J. Am. Chem. Soc. **132**, 9499 (2010).
[11] R. Czerwieniec, M. J. Leitl, H. H. H. Homeier, and H. Yersin, Coord. Chem. Rev. **325**, 2 (2016).
[12] M. Z. Shafikov, A. F. Suleymanova, R. Czerwieniec, and H. Yersin, Chem. Mater. **29**, 1708 (2017).
[13] W.-P. To, D. Zhou, G. So Ming Tong, G. Cheng, C. Yang, and C.-M. Che, Angew. Chem., Int. Ed. **129**, 14224 (2017).
[14] J. Fernandez-Cestau, B. Bertrand, M. Blaya, G. A. Jones, T. J. Penfold, and M. Bochmann, Chem. Commun. **51**, 16629 (2015).
[15] J. Gibson, A. P. Monkman, and T. J. Penfold, ChemPhysChem **17**, 2956 (2016).

[16]M. K. Etherington, J. Gibson, H. F. Higginbotham, T. J. Penfold, and A. P. Monkman, Nat. Commun. **7**, 13680 (2016).
[17]M. K. Etherington, F. Franchello, J. Gibson, T. Northey, J. Santos, J. S. Ward, H. F. Higginbotham, P. Data, A. Kurowska, P. Lays Dos Santos *et al.*, Nat. Commun. **8**, 14987 (2017).
[18]C. M. Marian, J. Phys. Chem. C **120**, 3715 (2016).
[19]I. Lyskov and C. M. Marian, J. Phys. Chem. C **121**, 21145 (2017).
[20]D. Di, A. S. Romanov, Le Yang, J. M. Richter, J. P. H. Rivett, S. Jones, T. H. Thomas, M. A. Jalebi, R. H. Friend, M. Linnolahti *et al.*, "High-performance light-emitting diodes based on carbene-metal-amides," Science **356**, 159 (2017).
[21]N. J. Turro, *Modern Molecular Photochemistry* (University Science Books, 1991).
[22]J. Fóller and C. M. Marian, J. Phys. Chem. Lett. **8**, 5643 (2017).
[23]S. Grimme and M. Waletzke, J. Chem. Phys. **111**, 5645 (1999).
[24]I. Lyskov, M. Kleinschmidt, and C. M. Marian, J. Chem. Phys. **144**, 034104 (2016).
[25]Y. Shao *et al.*, Mol. Phys. **113**, 184 (2015).
[26]C. Adamo and V. Barone, J. Chem. Phys. **110**, 6158 (1999).
[27]F. Weigend and R. Ahlrichs, Phys. Chem. Chem. Phys. **7**, 3297 (2005).
[28]D. Andrae, U. Häußermann, M. Dolg, H. Stoll, and H. Preuß, Theor. Chem. Acc. **77**, 123 (1990).
[29]S. Hirata and M. Head-Gordon, Chem. Phys. Lett. **314**, 291 (1999).
[30]A. Klamt and G. J. Schüürmann, J. Chem. Soc., Perkin Trans. 2 **5**, 799–805 (1993).
[31]A. Klamt, J. Phys. Chem. **100**, 3349 (1996).
[32]G. Te Velde, F. M. Bickelhaupt, E. J. Baerends, C. Fonseca Guerra, S. J. A. van Gisbergen, J. G. Snijders, and T. Ziegler, J. Comput. Chem. **22**, 931 (2001).
[33]C. Fonseca Guerra, J. G. Snijders, G. te Velde, and E. J. Baerends, Theor. Chem. Acc. **99**, 391 (1998).
[34]E. Jan Baerends *et al.*, *ADF2017, SCM, Theoretical Chemistry* (Vrije Universiteit, Amsterdam, The Netherlands, 2017), https://www.scm.com.
[35]E. van Lenthe, E. J. Baerends, and J. G. Snijders, J. Chem. Phys. **99**, 4597 (1993).
[36]E. van Lenthe, E. J. Baerends, and J. G. Snijders, J. Chem. Phys. **101**, 9783 (1994).
[37]E. van Lenthe, A. Ehlers, and E.-J. Baerends, J. Chem. Phys. **110**, 8943 (1999).
[38]E. van Lenthe and E. J. Baerends, J. Comput. Chem. **24**, 1142 (2003).
[39]D. P. Chong, E. van Lenthe, S. van Gisbergen, and E. J. Baerends, J. Comput. Chem. **25**, 1030 (2004).
[40]D. P. Chong, Mol. Phys. **103**, 749 (2005).
[41]M. Pápai, T. J. Penfold, and K. B. Moller, J. Phys. Chem. C **120**, 17234 (2016).
[42]G. Capano, T. J. Penfold, U. Röthlisberger, and I. Tavernelli, Chimia **68**, 227 (2014).
[43]J. Eng, C. Gourlaouen, E. Gindensperger, and C. Daniel, Acc. Chem. Res. **48**, 809 (2015).
[44]J. E. Subotnik, S. Yeganeh, R. J. Cave, and M. A. Ratner, J. Chem. Phys. **129**(24), 244101 (2008).
[45]M. H. Beck, A. Jäckle, G. A. Worth, and H.-D. Meyer, Phys. Rep. **324**(1), 1–105 (2000).